International Journal of Biological Macromolecules 321 (2025) 146279

Contents lists available at ScienceDirect

International Journal of Biological Macromolecules

journal homepage: www.elsevier.com/locate/ijbiomac

Optimized microfluidic blow spinning process for single-step manufacturing of crosslinked chitosan nanofilaments using a quality-by-design approach

Ana Filipa Matos [a], Alessio Pricci [b], Serena Benedetti [a], Mattia Tiboni [a], Annalisa Aluigi [a,*], Luca Casettari [a]

[a] *Department of Biomolecular Sciences, University of Urbino Carlo Bo, Piazza del Rinascimento, 6, Urbino, PU 61029, Italy*
[b] *Department of Mechanics, Mathematics and Management (DMMM), Polytechnic University of Bari, Bari, Italy*

ARTICLE INFO

Keywords:
Chitosan
Microfluidic blow spinning
Crosslinking
Computational fluid dynamics
Design of Experiment

ABSTRACT

Nanofibrous patches composed of chitosan (CS) present promising solutions for wound healing by supporting cell growth and enabling controlled drug release. This study introduces a new single-step microfluidic blow-spinning process that blends CS with polyethylene oxide (PEO) and crosslinks it with tripolyphosphate (TPP) using a series of laminar flow chips integrated into a blow-spinning apparatus. The microfluidic mixing between PEO and CS solutions at different concentrations was simulated with computational fluid dynamics (CFD). This manufacturing process was optimized through a Design of Experiment Approach (DOE) consisting of a 2^4 full-level screening design followed by a Box-Behnken optimization design. Design spaces correlating the CS concentration, the flow rate ratio between TPP solution and CS/PEO solution, and the air pressure with the filaments' mean diameter, diameter distribution, and deposition time were defined. These design spaces were used to select the process conditions suitable to obtain filaments with a mean diameter of 295 nm, a diameter distribution width approaching 150 nm, and a deposition time higher than 30 min. The good agreement between the predicted and experimental properties validated the design spaces. The crosslinked sample presented a higher water stability than the uncrosslinked one, retaining the fibrous structure with a swelling ratio of 470 ± 60 %. The cytotoxicity test on HaCaT keratinocyte cells showed no significant reduction in cell viability or protein content, confirming the patch's safety and compatibility for biomedical applications.

1. Introduction

Nanofibrous non-woven patches composed of natural polymers have shown great potential for biomedical applications, especially as wound dressings [1,2]. Their structural resemblance to the native extracellular matrix (ECM), characterized by high porosity and a large surface-to-volume ratio, supports cell adhesion, proliferation, migration, and differentiation [3,4]. Additionally, the fibers can be loaded with active pharmaceutical ingredients, enabling controlled and sustained drug release or other bioactive molecules to modulate tissue regeneration and repair.

Microfluidic blow spinning (MBS) combines microfluidics with solution blow spinning techniques to produce nanofibers [5]. First, the solutions are blended into the microfluidic device, which allows precise control over the material mixture. Then, the blended solution is ejected through a small nozzle toward a collector while subjected to a pressurized airflow, which stretches and solidifies the solution into fibers [6]. Compared to other methods used to produce nanofibrous patches (e.g., electrospinning, which relies on an electrostatic force to overcome surface tension and form the fibers, centrifugal spinning, which uses high-speed rotation to generate centrifugal force and extrude polymer solutions through nozzles [7] and solution blow spinning, which employs a high-pressure gas stream to stretch polymer solutions into fibers [8]), MBS has recently been considered a valid alternative [6]. It offers several advantages, including improved safety, avoidance of solvents with high dielectric constants, greater industrial scalability, precise control over the diameter and structure of the fibers, and the ability to integrate the solution preparation phase into a continuous in-process workflow, overcoming solution storage instability [9,10].

Chitosan (CS) is a natural polymer widely used in biomedical

---

* Corresponding author.
E-mail address: annalisa.aluigi@uniurb.it (A. Aluigi).

https://doi.org/10.1016/j.ijbiomac.2025.146279
Received 29 May 2025; Received in revised form 10 July 2025; Accepted 22 July 2025
Available online 24 July 2025
0141-8130/© 2025 The Authors. Published by Elsevier B.V. This is an open access article under the CC BY-NC-ND license (http://creativecommons.org/licenses/by-nc-nd/4.0/).

applications for its biodegradability and biocompatibility, as well as bioadhesiveness, antimicrobial, and hemostatic activities [11,12]. Moreover, it presents a great ability to bind negatively charged bioactive molecules due to the presence of active amino and hydroxyl groups in the molecular structure [13].

Despite CS advantages, the processing through spinning to prepare nanofibrous patches remains challenging due to the polymer's structural rigidity and hydrophilic nature that affects the stability of spun samples in physiological aqueous environments. To address these challenges, CS can be blended with other polymers.

Poly(ethylene oxide) (PEO) is a linear water-soluble polymer with excellent spinnability, often used to improve the spinnability of CS [14,15]. The advantages of using PEO over other polymers like PVA stem from its high chain flexibility, which facilitates the formation of continuous filaments, as well as its ease of dissolution in various solvents at room temperature (including acidic water). Good miscibility between CS and PEO can be achieved using concentrated acidic solvents such as trifluoroacetic acid or 50–90 % acetic acid [16]. However, when concentrated acids are used, the resulting patch must be purified before application, which could hinder an in situ application.

Several crosslinking strategies are also commonly used to improve the stability of nonwoven CS-based patches. For example, chemical methods through covalent bonds [17], ionotropic methods by electrostatic interactions [18] to ultraviolet (UV) light [17,19]. Tripolyphosphate (TPP) is an anionic crosslinker widely used in chitosan-based biomaterials due to its effectiveness and biocompatibility [18,20,21], but the simple addition to chitosan solutions before spinning can lead to instantaneous gelation, resulting in CS precipitation [22]. As a result, crosslinking with TPP is usually performed in a post-processing phase by dipping the CS based spun sample into TPP solutions [23,24]. Nevertheless, this two-step approach is significantly influenced by pH conditions which can impact the efficiency of crosslinking [23,24]. Additionally, it presents challenges for industrial-scale production, as it elevates manufacturing costs, extends processing times, and produces wastewater that necessitates treatment or disposal [25].

In this work, we hypothesized that a novel MBS-based method can enable the manufacturing of crosslinked CS-based nanofibrous patches with tunable morphological properties for wound healing applications in one single step, eliminating the need for a separate post-spinning crosslinking bath and thereby minimizing wastewater generation.

Computational Fluid Dynamics (CFD) is a simulation-based technique used to model how fluids flow and mix, based on the physics of fluid motion [26]. As a result, multiphase CFD was used to simulate the mix of CS and PEO solutions inside the blending unit to correlate the results with their rheological behaviors, ultimately affecting the solution's spinnability.

As the newly developed MBS technique is a complex process, the Critical Quality Attributes (CQAs) of the patches (e.g., morphology and production yield) are influenced by several parameters (e.g., air pressure, concentration, and flow rate of the solutions in the chips). Therefore, a Quality by Design (QbD) approach was employed to develop a robust process that ensures reproducible production of patches with the desired properties using adequate process parameters. Design of Experiment (DOE) was the statistical method used to identify the key factors significantly impacting the patch morphology and production rate. By simultaneously varying the process parameters, DOE enables a comprehensive analysis of their interactions and impact on the manufacturing process while reducing the number of tests necessary [27,28]. A two-level full factorial design was utilized as a screening method to identify the key factors that affect the responses and delineate the spinnability domain [29]. Then, the Box-Behnken Design combined with the Response Surface Methodology (RSM) was employed to create the predictive regression models that define the relationships between multiple process factors and responses (design spaces), enabling the identification of optimal conditions for the desired outcome [28]. Predictive modeling and an experimental confirmation approach validated the developed design spaces. The effect of crosslinking on the spun solutions' rheological behavior and the patches' chemical structure, morphology, and water stability was also investigated.

Finally, to evaluate the potential applications of the developed CS-based patches in wound healing, preliminary studies about their toxicity toward a model of epidermal cells (HaCaT) were carried out using the water-soluble tetrazolium (WST)-8 and sulforhodamine B (SRB) assays.

2. Materials and methods

2.1. Materials

CS with a molecular weight 150 kDa and a degree of deacetylation 90 % (ChitoClear 3255) was purchased from Chitoclear Primex (Siglufjordur, Iceland), PEO of 900 kDa was kindly supplied by DuPont (Wilmington, DE, USA), and TPP was purchased from Sigma-Aldrich (St. Louis, MO, USA). All other chemicals were purchased from Thermo Fischer Scientific.

2.2. Preparation of CS, PEO, and TPP solutions

CS was dissolved at the desired concentration (% *w/V*) in an aqueous solution of acetic acid at 1 % (*V*/V) and maintained under stirring overnight at room temperature (RT). PEO was dissolved in distilled water at a concentration of 2 % (*w/V*) and maintained under stirring overnight at RT. Finally, the TPP was dissolved in distilled water at the desired concentration (% *w/V*) and maintained under stirring at RT until fully dissolved.

2.3. Microfluidic blow spinning (MBS) apparatus

The new MBS apparatus (Fig. 1a) developed consists of two series-connected microfluidic chips with a Y-shaped microchannel. The first chip (blending unit) is where CS is blended with PEO under diluted acidic conditions, while the second chip (crosslinking unit) is where the ionic crosslinking with TPP occurs (Fig. 1b). The output of the crosslinking unit is a needle connected to the inner part of a coaxial spinneret, whose outer channel is used to supply compressed air **(**Fig. 1c). The coaxial spinneret is inserted in a chamber (Fig. 1a) containing the collector, where the resulting CS/PEO/TPP solution is blow-spun and the filaments are deposited (Fig. 1c). The chamber is heated to facilitate the solvent evaporation during the filament stretching.

2.4. Design of experiments (DOE) of spinning process

The flow rate of PEO and CS solutions in the blending unit was set at 0.1 mL/min, presenting a total flow rate of 0.2 mL/min. The spinneret-to-collector distance and chamber temperature were fixed at 30 cm and 40 °C, respectively. All other process parameters, including CS and TPP solution concentrations, air pressure, and flow rate ratio (FRR) in the crosslinking unit (FRR_{CR}, defined as the ratio between the TPP solution flow rate and the CS/PEO solution flow rate maintained at 0.2 mL/min), were varied according to a DOE approach. The DOE consisted of a Screening Design followed by an Optimization Design, performed using Design Expert Stat-Ease® (v. 23.1) software.

2.4.1. Screening design

A two-level full factorial design (2^4 factorial design) was used to evaluate the process factors' effects, namely CS concentration, FRR_{CR}, TPP concentration, and air pressure. The two levels assigned to each factor are reported in Table S1. The screening design required 16 experiments, following the 2^4 factorial design. Three blocks of 16 experiments were performed with different randomizations to ensure reliability, resulting in 48 experiments (**Table S2**).

The spinnability was considered as the response and was assessed

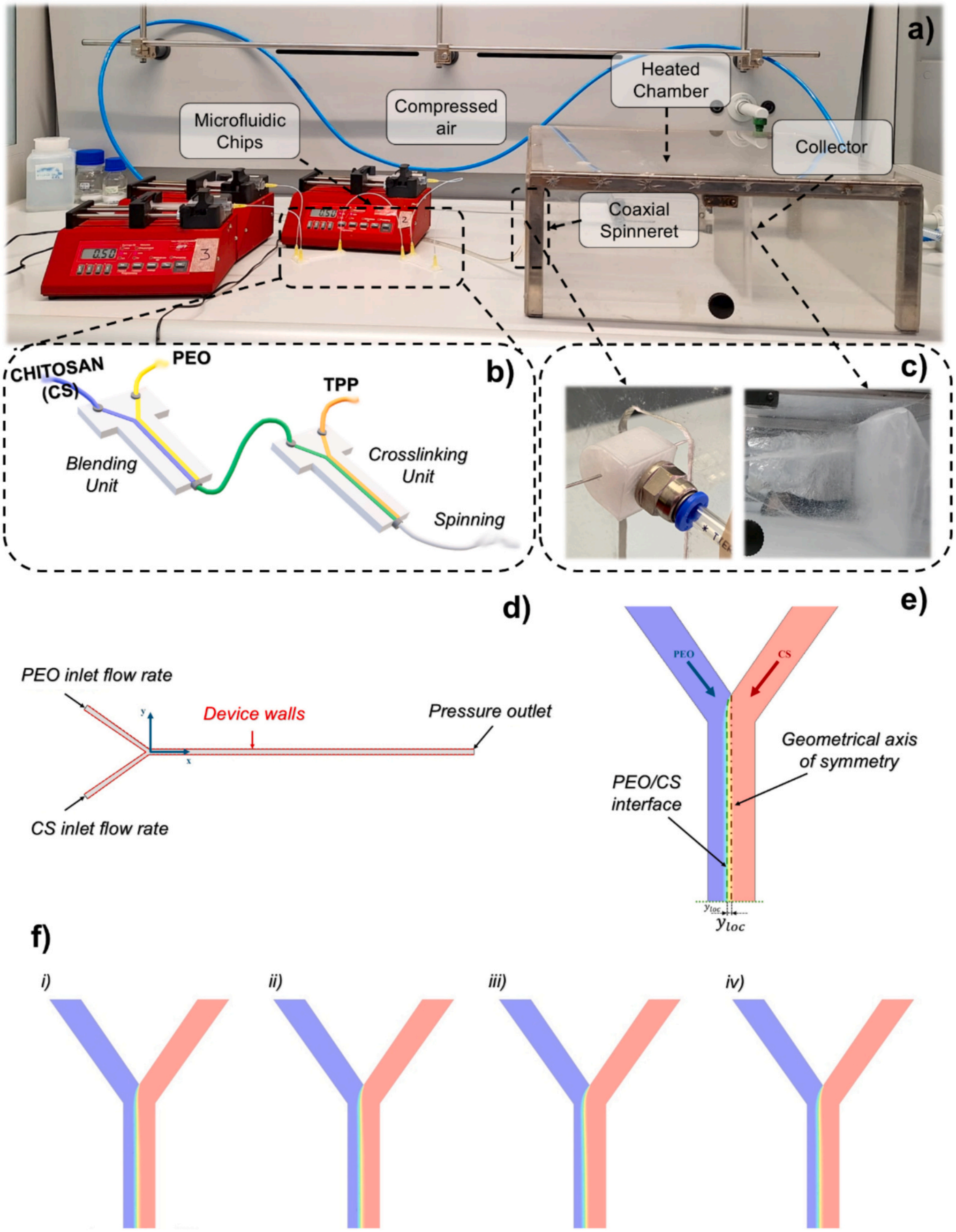

Fig. 1. *a) Set-up of the microfluidic blow spinning (MBS) apparatus, b) schematic detail of the blending unit chip and crosslinking unit chip disposed in serie, c) detail of the spinneret (Domínguez* et al., *2021) and collector; d) Computational 2D domain, reference system and boundary conditions used for the CFD studies, e) CFD simulation of PEO and CS fluid flow in the blending chip, with indication of the PEO/CS interface location (y_{loc}), f) CFD simulation of the fluid flow in the blending unit of PEO and CS at i) 2.5 % (w/V), ii) 3 % (w/V), iii) 3.5 % (w/V) and iv) 4 % (w/V), blue: PEO and red: CS.*

using the following scoring system: 1 – not spinnable (solution dripping or microchannel clogging), 2 – poor spinnability (spinning lasted less than 1 min due to clogging in the crosslinking unit), 3 – spinnable (spinning with occasional drops), 4 – highly spinnable.

2.4.2. Optimization design

A Box-Behnken design was used to perform the optimization, and the selected factors were the concentration of CS solution, the $FRR_{CR,}$ and the pressure. Based on the results obtained in the screening design, the range for each factor was defined, while the TPP concentration was fixed at 9 % (*w*/w). The actual and coded values for each factor are summarized in Table 1. The mean diameter and the width of the diameter distribution, as well as deposition time, were considered as response

Table 1
Actual and coded values of the selected factors for the Box-Behnken design.

	Coded Value		
	−1	0	1
	Actual Value		
A. Chitosan concentration (% w/V)	2	2.5	3
B. FRR_{CR}	0	0.5	1
C. Pressure (Bar)	1	1.5	2

Table 2

Experimental runs were performed according to the Box-Behnken design and the respective results.

Std	Run	Chitosan concentration % (w/V)	FRR_{CR} mL/min	Pressure Bar	Fiber diameter nm	Fiber Diameter Distribution width (w) nm	Deposition Time min
1	13	2	0	1.5	402	148	60
2	6	3	0	1.5	383	150	60
3	1	2	1	1.5	368	195	20
4	14	3	1	1.5	247	143	13
5	2	2	0.5	1	348	212	18
6	3	3	0.5	1	355	183	15
7	9	2	0.5	2	341	158	23
8	15	3	0.5	2	238	118	18
9	5	2.5	0	1	414	233	60
10	7	2.5	1	1	436	292	15
11	10	2.5	0	2	500	240	60
12	12	2.5	1	2	324	272	15
13	8	2.5	0.5	1.5	280	156	23
14	4	2.5	0.5	1.5	274	180	20
15	11	2.5	0.5	1.5	232	118	23

variables. The factors and their corresponding levels are combined according to Table 2 (Std Column) and are randomly executed in the sequence specified in the Run Column.

2.5. Physico-chemical characterization

2.5.1. Rheological properties of solutions

Shear viscosity was measured by gradually increasing the shear rate from 0.1 to 1000 s^{-1} at 25 °C using a stress-controlled rheometer (MCR302e, Anton Paar, Graz, Austria) equipped with a cone-plate geometry (CP50–2: cone angle 2°, diameter 49.96 mm, truncation 48 μm). A cap was used to minimize solvent evaporation during the measurements.

2.5.2. Scanning electron microscopy (SEM) analysis

The morphology of the samples was observed by scanning electron microscopy (SEM). The samples were gold sputter-coated and observed using an ESEM Quanta 200 FEG (FEI, Hillsboro, OR, USA), operating at an acceleration voltage of 20 kV. For each sample, 100 measurements of different nanofiber diameters were taken from the collected SEM images using ImageJ software (National Institutes of Health, Bethesda, MD, USA). The obtained diameter distribution was fitted to a Gaussian equation (Eq. 1) using the Origin Pro software (OriginLab, Northampton, MA, USA). The center x_c and the width w of the Gaussian function were used to estimate the filaments' mean diameter and distribution width characterizing the patch, respectively (**Fig. S1**).

$$y = y_0 + \frac{A}{w\sqrt{\pi/2}} e^{-2\frac{(x-x_c)^2}{w^2}} \tag{1}$$

2.5.3. Attenuated Total reflection Fourier transformed infrared spectroscopy (ATR-FTIR)

To identify the functional groups on the nanofiber samples, the infrared spectra were acquired using ATR-FTIR (Attenuated Total Reflection – Fourier Transform Infrared Spectroscopy) (PerkinElmer, Waltham, MA, USA) in the wavenumber range of 500–4000 cm^{-1}, with a resolution of 2 cm^{-1} and 32 scans.

2.5.4. Water stability

To evaluate the water stability, dried samples (w_{dry1}/mg) were immersed in distilled water (pH 7.0) for 24 h at 37 °C. After immersion, the samples were centrifuged at 4000 rpm for 15 min at 25 °C, and the supernatant was removed. Then, the remaining samples were dried again at 37 °C for 24 h and weighed (w_{dry2}/mg). The water stability was calculated using the following equation (Eq. 2):

$$Water\ stability\ (\%) = \frac{w_{dry2}}{w_{dry1}} \times 100 \tag{2}$$

2.6. CFD modeling of the fluid flow of PEO and CS in the blending unit

The fluid flow of PEO and CS in the microfluidic chip of the blending unit was simulated with the software ANSYS Fluent *v*.19.2, which is based on the finite volume method.

Although the software performs multiphase CFD simulations using simplified approaches, such as the widely adopted volume-of-fluid and mixture models, the Eulerian model was chosen for its completeness. The choice was further justified by the complexity of the non-Newtonian fluid flow features of PEO and CS (**Fig. S2**).

The Eulerian model solves a set of momentum and continuity equations for each fluid phase. However, a single pressure field is shared by all phases.

Given the volumetric fluid fraction of the i-th α_i phase, the corresponding volume is (Eq. 3):

$$V_i = \int_V \alpha_i dV \tag{3}$$

For an arbitrary number of substances (*N* phases), the overall fluid fraction in each computational cell must be unit (Eq. 4):

$$\sum_{i=1}^{N} \alpha_i = 1 \tag{4}$$

The continuity equation for the i-th phase can be written as follows (Eq. 5):

$$\frac{\partial(\rho_i \alpha_i)}{\partial t} + \vec{\nabla} \bullet (\rho_i \alpha_i \vec{u_i}) = 0 \tag{5}$$

Here, ρ_i and $\vec{u_i}$ are the density and velocity of the i-th phase, respectively.

Momentum equation for the i-th phase is (Eq. 6):

$$\frac{\partial(\rho_i \alpha_i \vec{u_i})}{\partial t} + \vec{\nabla} \bullet (\rho_i \alpha_i \vec{u_i}\, \vec{u_i}) = -\alpha_i \overrightarrow{\nabla p} + \vec{\nabla} \bullet \bar{\bar{\tau_i}} + \alpha_i \rho_i \vec{g} \tag{6}$$

is the pressure field shared by the two phases, $\bar{\bar{\tau_i}}$ the i-th phase stress tensor and $\vec{g}$ gravity acceleration.

The exact formulation of the stress tensor $\bar{\bar{\tau_i}}$ depends on the rheological features of the i-th phase. Both PEO and CS at different concentrations have shown non-Newtonian features (**Fig. S2**); the expression for $\bar{\bar{\tau_i}}$ at varying CS concentrations is found by considering each fluid as a generalized Newtonian fluid. Therefore, the stress tensor $\bar{\bar{\tau_i}}$ can be expressed as a function of the shear rate tensor $\bar{\bar{D_i}}$ (Eq. 7)

$$\bar{\bar{\tau_i}} = 2\eta_i(\dot{\gamma}_i)\bar{\bar{D_i}} \tag{7}$$

Here, $\eta_i(\dot{\gamma})$ is the dynamic viscosity and the shear rate (Eq. 8):

$$\dot{\gamma}_i = 2\sqrt{D_i^{=} : D_i^{=}} \tag{8}$$

The dynamic viscosity of the i-th component $\eta_i(\dot{\gamma})$ has been specified accordingly to the Cross-WLF rheological model (Eq. 9):

$$\eta_i(\dot{\gamma}) = \frac{\eta_0}{1 + \left(\frac{\eta_0 \dot{\gamma}}{\tau^*}\right)^{1-n}} \tag{9}$$

Here, η_0 is zero-shear dynamic viscosity, $\dot{\gamma}$ the shear rate, n the power-law index and τ^* the critical stress level at the transition to shear-thinning behavior.

The values of these quantities depend on the i-th phase, and they have been fitted to rheological measurements. Their values have been reported in **Table S3.**

Through the applications of Eqs. (5) and (6) to each phase, the fluid-fluid interaction is solved, and the interface between the two fluids is accurately tracked.

The boundary conditions employed to study the fluid flow in the mixing device are as follows (Fig. 1d): a) PEO and CS inlets: flow rate equal to 0.1 mL/min; b) device walls: no-slip boundary condition; and c) outlet: relative pressure set equal to zero.

A phase-coupled SIMPLE algorithm was used to solve pressure-velocity coupling. Additionally, the least squares cell-based method was employed for spatial gradient discretization, while second-order upwind schemes were chosen for momentum and volume fraction calculations.

Continuity and momentum equations were solved by setting the residual of each variable equal to $1e^{-6}$, to provide appropriate accuracy in PEO/CS interface tracking.

2.7. Cytotoxicity

The cytotoxicity of the patch was evaluated in the human keratinocyte cell line HaCaT (CLS-Cell Lines Service GmbH, Eppelheim, Germany), maintained in Dulbecco's Modified Eagle Medium (DMEM) supplemented with 10 % fetal bovine serum, 2 mM L-glutamine, and 1 mM sodium pyruvate (Sigma-Aldrich, Milan, Italy). Cells (5×10^3/well) were seeded in 96-well plates and left to adhere for 24 h at 37 °C with 5 % CO_2. Meanwhile, patch specimens (0.5×0.5 cm^2, approximately 2.5 mg) were sterilized using UV radiation and incubated in 1.0 mL of complete DMEM medium at 37 °C with 5 % CO₂ for 24 h to prepare the specimen extract, following ISO 10993-5 guidelines [30]. After incubation, the culture medium in the 96-well plate was replaced with 100 μL of either the negative control (complete medium), positive control (10 % DMSO in complete medium), or patch extract at three different dilutions (100 %, 50 % and 25 %), in triplicate After 24 h of incubation, the cell viability was evaluated using the WST-8 assay for metabolic activity and the SRB assay for total protein content [31]. Briefly, test compounds were removed, and fresh medium containing WST-8 (Merck, Italy) was added to each well. Color development was evaluated after 2 h at 450 nm in a multiwell plate reader (Multiskan FC, Thermo Scientific). The SRB test was then immediately performed in the same 96-well plate: cells were fixed with 50 % trichloroacetic acid and stained with 0.4 % SRB (Merck, Italy); protein-bound SRB was solubilized with 10 mM Tris and the absorbance read at 570 nm. Data were expressed as cell viability (%) versus control cells, and results presented as mean ± standard deviation of three independent experiments. Differences between groups (negative control, positive control, and patch extractive medium) were analyzed using the one-way analysis of variance test (ANOVA) followed by Tukey's test for multiple comparisons. A *p-value* < 0.05 was considered statistically significant. According to ISO10993-5, materials were considered biocompatible as the cell viability of the sample extract was higher than 70 % of the control [30]. Morphological analysis of the cells was carried out by a phase-contrast microscope (Olympus IX50, Segrate, Italy) using the 10× magnification; images were acquired by a ToupCam camera equipped with ToupView control software (ToupTek Europe).

2.8. Statistical analysis

A standard analysis of variance (ANOVA) was performed to select the significant factors in a multi-factor model, considering a statistical significance level of 5 %. The model validation correlating the input factors with the results (output data) was based on *p-value*, *F-value*, and regression coefficients R^2, adjusted R^2 (adj-R^2), and predicted R^2 (pred-R^2). The regression model was considered significant if *p-value* < 0.05, and the best-fitting model for each response was selected based on the highest adj-R^2 and a difference between pred-R^2 and adj-R^2 of less than 0.2. For each output, the coded equation (based on coded factor levels) was used to identify the factors and the interactions that mainly influence the results. Instead, the actual equation (based on actual factor levels) was employed to generate response surface plots illustrating the relationships between process factors and responses.

3. Results and discussion

3.1. Study of the solution flow in the microchannel of the blending unit chip

As shown in Fig. 1b, the CS dissolved in acetic acid 1 % (*w/V*) was mixed with PEO aqueous solution in the blending unit. To simplify, the PEO concentration was kept constant at 2 % (*w/V*), while CS solutions were evaluated at varying concentrations (2.5 %, 3 %, 3.5 %, 4 % w/*V*). The flow rates of both PEO and CS solutions were maintained at 0.1 mL/min.

Before analyzing the interaction between CS and PEO at different concentrations, the optimal size of the computational mesh was determined. The position of the interface location along the y direction of Fig. 1d between the two phases was chosen as the target variable (indicated as y_{loc} in Fig. 1e). The abovementioned location corresponds to a fluid fraction of each phase, α_i, equal to 0.5. For the grid-independence study, the 2.5 % (w/*V*) CS concentration has been chosen.

Different grid resolutions were used for this purpose (Table 3). As highlighted in Table 3, the position of the CS/PEO interface does not vary when employing mesh elements with a resolution of 50 μm. Therefore, this number was chosen for further computations under the remaining values of CS concentrations (see also **Tables S4, S5,** and **S6**). Then, the position of the fluid-to-fluid interface was studied at varying CS % (*w/V*) (Fig. 1f). The position of the interface is modified by the CS % (*w/V*). At low concentrations, it is more symmetrical (y_{loc} =103.19 μm, see Table 3). The fluid-to-fluid surface cannot be exactly symmetric because of the viscosity difference between the two phases (**Fig. S2**). This difference tends to increase when considering higher CS % (w/V). In fact, y_{loc} increases to 115.94 μm, 136.13 μm and 162.05 μm, when considering CS % (w/V) equal to 3, 3.5 and 4, respectively.

The CFD results suggest that viscosity-induced interface displacement can affect the degree of polymer interpenetration of the solution entering the crosslinking unit. This, in turn, may influence the final filament formation by altering the homogeneity and chain entanglement of the blend entering the crosslinking unit, and making final filament

Table 3
2.5 % (w/V) CS / PEO interface position at different values of grid resolutions. Percentages refer to the deviation with respect to 50 μm grid resolution result.

Grid resolution (μm)	Cell total count (−)	Interface position, y_{loc} (μm)
25	338.606	102.72
50	104.666	103.19 (+0.46 %)
75	51.840	115.14 (+12.09 %)
100	32.278	113.23 (+10.23 %)
150	17.303	113.98 (+10.96 %)

ejection practically impossible because of the too high viscosity.

3.2. *Definition of the spinnability area*

The MBS process is influenced by various parameters, resulting in a multidimensional space of variables for fiber production and optimization. This includes characteristics of the polymers (e.g., molecular weights and deacetylation degree), spinning solution viscosity, process parameters (e.g., total flow rate defined as the sum of the different phases' flow rate, FRR, air pressure, and spinneret-to-collector distance), and environmental conditions (e.g., temperature and relative humidity of the surrounding atmosphere). Thus, preliminary spinning tests were carried out to establish the conditions necessary to produce filaments. Subsequently, a screening design was performed to determine the suitable range of process parameters for optimization. **Table S1** presents the factors and corresponding levels considered in the 2^4 full factorial screening design. The full factorial design was selected as the screening tool to allow a comprehensive assessment of critical factors impacting the fiber formation, providing a robust foundation to identify the spinnable domain within the new one-step manufacturing process. Moreover, with only four factors under investigation, the experimental workload remained practical and manageable [32].

Since jet ejection was not possible with the CS solution 4 % (*w/V*) due to its high viscosity, the low and high levels of CS concentration were set at 2.5 % and 3.5 % (w/V), respectively.

The results (**Table S2**) were fitted to a multivariable linear equation (**Equation a in Table S7**). Among the evaluated factors, only CS concentration and FRR_{CR} significantly affected spinnability, presenting a *p-value* < 0.05 (**Table S7**). Consequently, the mathematical model was reduced by removing the non-significant factors (**Equation b in Table S7**). Based on the coefficients of the coded equation, spinnability improved as CS concentration and FRR_{CR} decreased, with a comparable contribution from both factors. As observed in literature, CS concentration, which directly influences solution viscosity, is expected to have a significant impact on spinnability, as nanofiber formation largely depends on polymer chain entanglements [33]. Higher CS concentrations present a higher number of chain entanglements and greater resistance to stretching, which supports stable fiber formation. However, excessively high concentrations can hinder solution spinning, leading to issues such as clogging, as the gas phase may not be able to draw out the highly viscous solution effectively [34].

The actual equation was used to determine the range of CS concentration and FRR_{CR} values that resulted in a spinnability score higher than 2.5 (Fig. 2). The selected optimization area for the process was defined within a CS concentration range from 2 to 3 % (*w/V*) and a FRR_{CR} range from 0 to 1 mL/min, with a fixed TPP concentration of 9 % (*w*/w).

3.3. *Effects of the input factors on the results and definition of the response surfaces*

The optimization results from the Box-Behnken design are summarized in Table 2. As expected, all 15 experimental conditions allowed spinning (Video 1), proving the successful establishment of the spinnable area and resulting in patches (Fig. 2) composed of continuous filaments with diameters ranging from 232 ± 118 nm to 500 ± 240 nm. Electrospinning techniques can produce thinner fibers, as reported by Jin An et al. [35], where the diameter ranged from 97 ± 13 nm to 117 ± 18 nm. However, the diameters observed in this study are consistent with those achieved using solution blow spinning. For example, Tien et al. reported fiber diameters between 270 ± 46 nm and 1057 ± 231 nm, while Szymańska et al. [9] obtained fibers with average diameters around 200–260 nm, depending on processing parameters. The differences are associated with the techniques, as the gas flow in solution blow spinning can produce fibers quickly and at high throughput, the mechanical stretching force is generally less intense and uniform than the electrostatic stretching in electrospinning, leading to thicker fibers on average [36,37]. Fig. 3 presents SEM images along with the diameter distribution of the obtained filaments.

The optimization of the manufacturing process requires defining the Design Space, represented by a set of response surfaces that correlate the input factors with results. A multivariable quadratic model was initially considered to establish these correlations (Table 4). The best-fitting polynomial model for each result was selected using the *p-values* and *F-values* (Table 4).

3.3.1. *Effects of the process parameters on the fiber diameter* ($\overline{D}$)

The peak of the Gaussian curve resulting from the diameter distribution fitting was considered the result D¯ (**Fig. S1**). As shown in Table 4, the complete quadratic model is significant, with a *p-value* $<$ 0.005 and an *F-value* of 16.23, indicating that there is only a 0.34 % probability that such a large *F-value* could occur due to noise. The R^2, adj-R^2, and pred-R^2 values are 0.9669, 0.9073, and 0.6894, respectively. Since the difference between pred-R^2 and adj-R^2 exceeds 0.2, a model

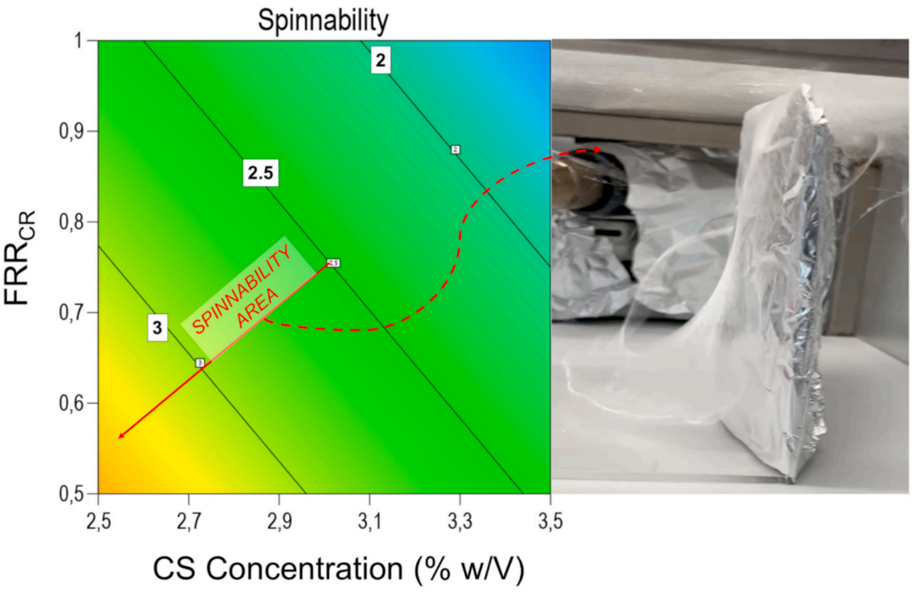

Fig. 2. Spinnability area defined through the screening design.

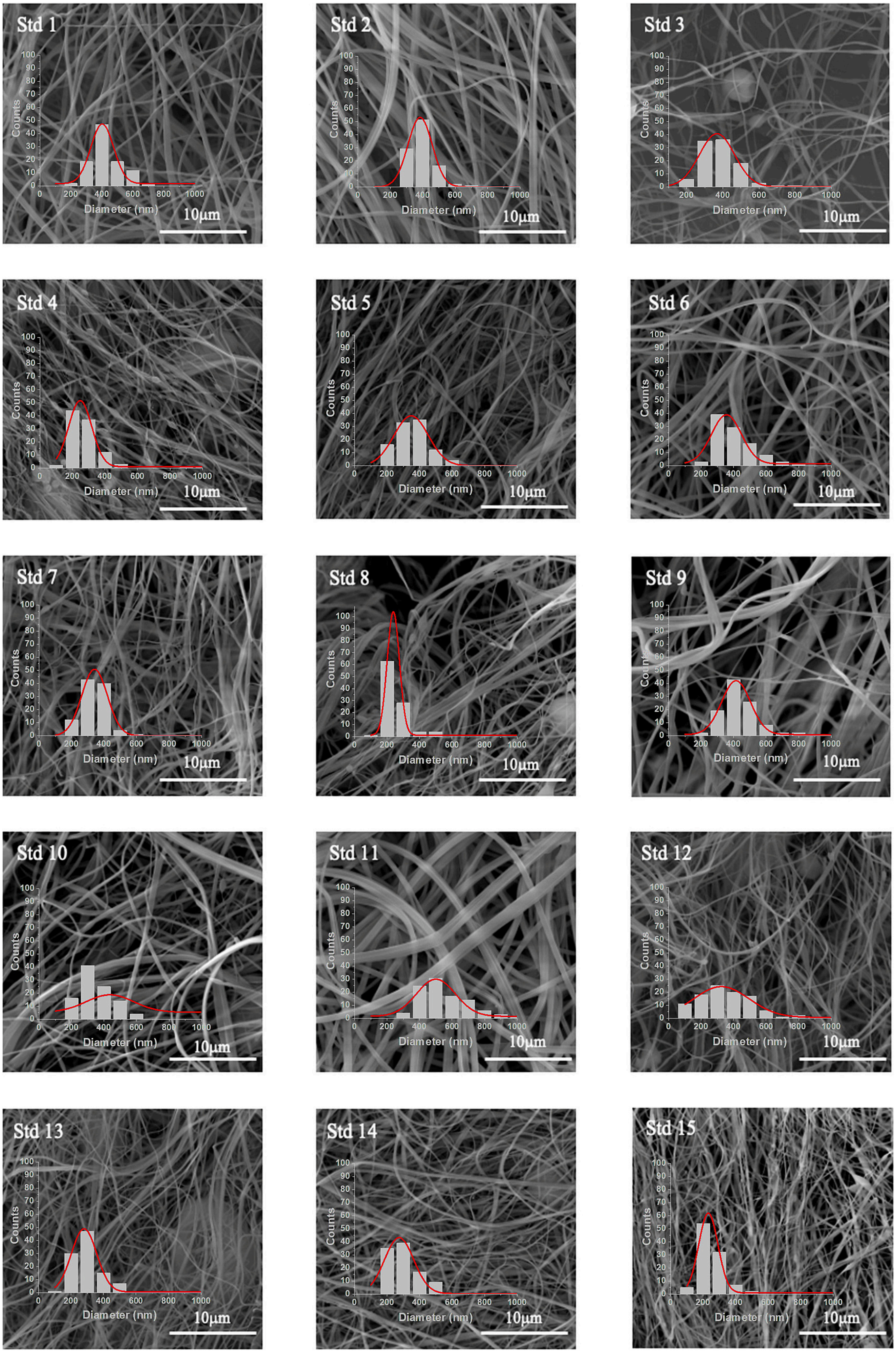

Fig. 3. SEM micrographs of spun samples and related diameters distribution.

Table 4
ANOVA results of the multivariable quadratic model applied to diameter $\overline{D}$, diameters distribution width (W) and deposition time (Optimization Design).

$Y = \beta_0 + \beta_{11}A^2 + \beta_{22}B^2 + \beta_{33}C^2 + \beta_1 A + \beta_2 B + \beta_3 C + \beta_{12}AB + \beta_{13}AC + \beta_{23}BC$

Source	*P- value*			F-value		
	$\overline{D}$ (nm)	W (nm)	Time (min)	$\overline{D}$ (nm)	Width (nm)	Deposition Time (min)
Model	0.0034	0.0388	< 0.0001	16.23	5.41	188.72
A	0.0173	0.1841	0.0289	12.25	2.37	9.22
B	0.0049	0.1507	< 0.0001	23.08	2.88	1283.98
C	0.0767	0.1482	0.1663	4.95	2.92	2.62
AB	0.0854	0.3682	0.1014	4.58	0.9774	4.02
AC	0.0692	0.8483	0.5917	5.32	0.0406	0.3279
BC	0.00889	0.642	1.0000	17.24	0.2443	0.0000
A^2	0.7036	0.0319	0.1907	0.1624	8.7	2.29
B^2	0.0007	0.0175	< 0.0001	56.17	12.17	376.06
C^2	0.0037	0.0093	0.0665	26.19	16.84	5.47

reduction was considered. Specifically, the term A^2 was removed from the equation as it was insignificant (*p-value* > 0.1). The resulting optimized mathematical model is more significant than the previous one, with higher adj-R^2 (0.9203) and pred-R^2 (0.7833), which are in reasonable agreement with a difference lower than 0.2. Furthermore, an *F-value* of 21.19 indicates that the probability of obtaining such a large *F-value* due to random noise is only 0.07 %. Table 5 presents the coded and actual equations of the optimized model, while the corresponding response surfaces are shown in Fig. 5a. The results confirm that FRR_{CR} and pressure are the factors that mainly influence the filament diameter.

In **Fig. S3 a**, the predicted versus actual values graph related to the refined model is reported. This graph helps to understand how good the model for prediction purposes is. As observed, the model did well for all the outputs.

3.3.2. *Effects of the process parameters on the fibers' homogeneity*

In this study, fiber homogeneity was evaluated by analyzing the width of the Gaussian peak fitted to the diameter distribution, with a narrower peak reflecting higher uniformity among the fibers (**Fig. S1**). According to the ANOVA analysis (Table 4), the complete quadratic model is statistically significant, with a *p-value* < 0.05 and an F-value of 5.41, implying only a 3.88 % probability that such a large *F-value* could result from noise. The R^2, adj-R^2, and pred-R^2 values are 0.9069, 0.7394, and 0.1817, respectively. Since the difference between pred-R^2 and adj-R^2 exceeds 0.2, a model reduction was considered. Based on *p-values*, only the quadratic terms (A^2, B^2, and C^2) were significant, but the linear terms A, B, and C were also retained in the refined mathematical model to maintain the hierarchy. Compared to the complete model, the refined model exhibits a higher adj-R^2 (0.7960), which is in reasonable agreement with pred-R^2 (0.6191), as their difference is below 0.2. Additionally, the model *F-value* of 10.11 indicates that the probability of obtaining such a large *F-value* due to noise is reduced to 0.23 %. The final coded equation in Table 5 suggests that pressure has the greatest influence on fiber diameters distribution width, followed by FRR_{CR} and CS concentration (Fig. 4b).

Table 5
Coded and actual equations of the refined mathematical models.

Response	Refined Mathematical Model
$\overline{D}$ (nm)	Coded Equation: $\overline{D} = 258.92 - 29.5A - 40.5B - 18.75C - 25.5AB - 27.5AC - 49.5BC + 93.38B^2 + 63.88C^2$ Actual Equation: $\overline{D} = 483 + 157A + 97.5B - 430C - 102AB - 110AC - 198BC + 373.5B^2 + 255.5C^2$
W (nm)	Coded Equation: $W = 151.33 - 14.88A + 16.37B - 16.5C - 42A^2 + 49.6B^2 + 58.3C^2$ Actual Equation: $W = -214.5 + 808.6A - 165.6B - 733C - 168A^2 + 198B^2 + 233C^2$
Deposition Time (min)	Coded Equation: $Time = 21.1 - 1.9A - 22.1B + 1C - 1.7AB + 17.7B^2 - 2C^2$ Actual Equation: $Time = 40.5 - 0.25A - 97.7B + 26.2C - 7AB + 70.9B^2 - 8C^2$

Regarding the prediction ability, the model is doing well, except for the outputs lower than 150 nm (**Fig. S3 b,** region highlighted with the red circle).

3.3.3. *Effects of the process parameters on the deposition time*

Deposition time is directly linked to clogging in the crosslinking unit. The complete quadratic model for deposition time is statistically significant (Table 4), with a model *F-value* of 188.72, indicating only a 0.01 % probability that such a large *F-value* could result from noise.

The model's R^2 and adj-R^2 and pred-R^2 values are 0.9971, 0.9918 and 0.9689, respectively. However, after removing the non-significant terms (AC, BC, and A^2), the adj-R^2 increases to 0.9922, confirming that the refined model provides a better fit. Additionally, the pred-R^2 value of 0.9849 is in reasonable agreement with adj-R^2, supporting the selection of the refined model as the best fit for deposition time. According to the coded equation, deposition time is primarily influenced by FRR_{CR}. In particular, the negative regression coefficient of FRR_{CR} indicates that deposition time increases as FRR_{CR} decreases (Fig. 4c). This result aligns with expectations, as a lower FRR_{CR} corresponds to a reduced degree of crosslinking, thereby decreasing the likelihood of clogging in the chip channel.

As observed in **Fig. S3c,** the prediction ability of the model is good enough in all the output regions.

3.4. *Study of the ionotropic crosslinking*

The ionotropic crosslinking of CS with the TPP consists in the establishment of interactions between positively charged amino groups of CS and negatively charges of TPP, as represented in Fig. 5a [18]. To evaluate the effect of crosslinking on the rheological behavior, the shear viscosity of crosslinked and uncrosslinked solutions exiting the crosslinking unit was compared. The crosslinked solution was prepared under the conditions of Std 15 ([CS] 2.5 %, FRR_{CR} 0.5 mL/min). The first uncrosslinked solution was prepared under Std-11 conditions, using the same CS concentration but without the TPP solution in the blending unit ([CS] 2.5 %, FRR_{CR} 0 mL/min). The second uncrosslinked solution (Std 11_DW) was prepared under the same conditions as Std 15, but TPP solution was replaced with distilled water to eliminate the effect of dilution in the shear viscosity ([CS] 2.5 %, FRR_{CR} 0.5 mL/min). **Table S8** summarizes the operating conditions used to prepare the crosslinked and uncrosslinked solutions and Fig. 5b presents the shear stress–shear rate curves for the three solutions.

The curves were fitted with the Herschel-Bulkley model described in Table 6, where *K* is the consistency index and *n* is the flow behavior index. A $n < 1$ indicates a shear-thinning behavior, and as it approaches 0, the shear-thinning becomes stronger. *K* reflects the apparent solution viscosity and is positively correlated with it [38].

As expected, all solutions (Std 11, Std 11_DW and Std 15) exhibited shear thinning behavior (Table 6), a desired behavior in spinning as the decrease in apparent viscosity in function of the shear rate facilitates the elongation of the polymer solution into nanofibers.

The uncrosslinked solution (Std 11) exhibited the highest consistency index, attributed to the greater concentration of chain entanglements due to the highest CS concentration. The higher consistency index implies greater resistance to jet stretching, thereby resulting in thicker filaments with a wider diameter distribution (**Fig. 5c and** f). In Std 11_DW solution, the dilution effect reduces the number of chain entanglements and therefore the consistency index (Table 6). This leads to

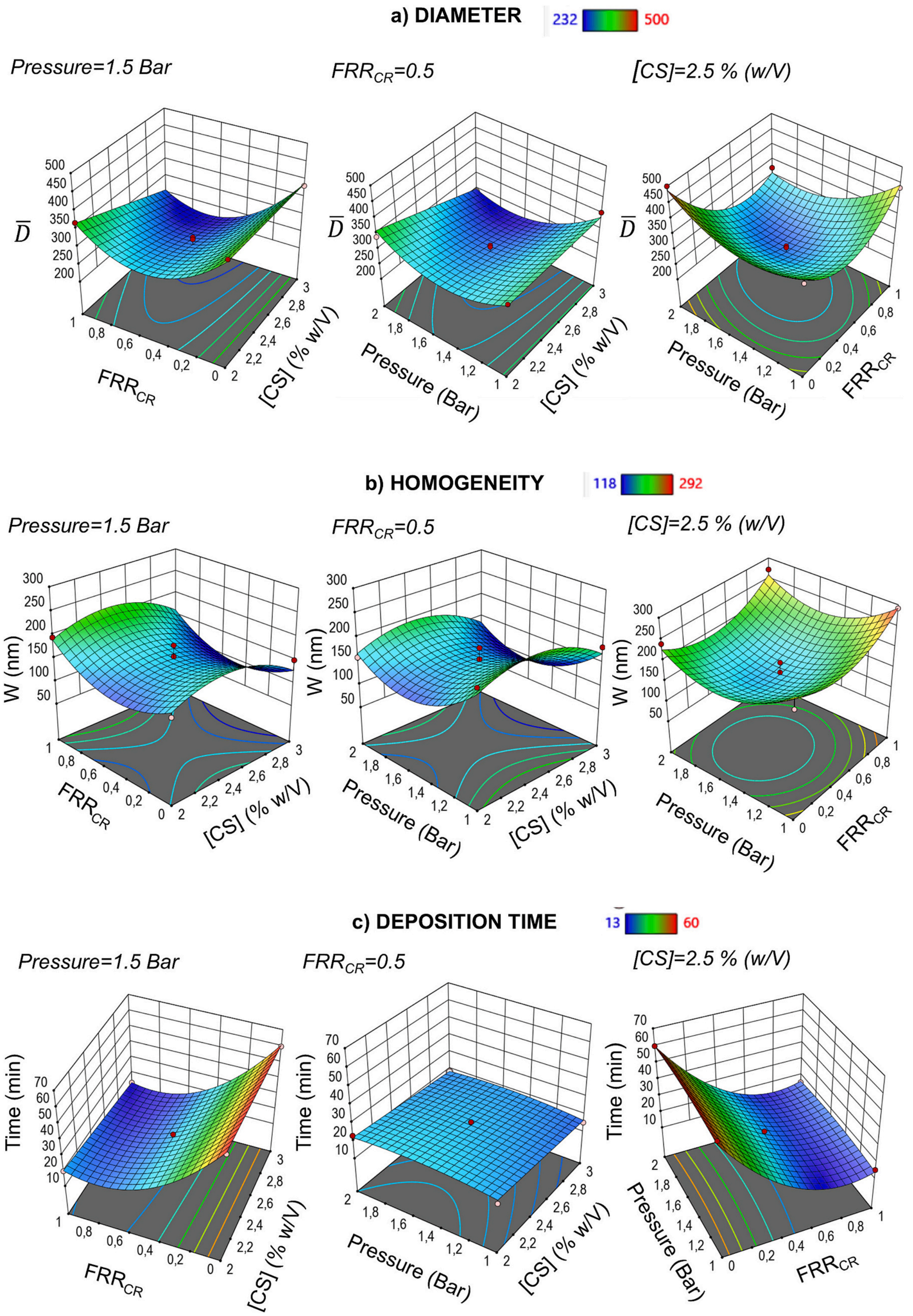

Fig. 4. Response surfaces correlating the process parameters with the filaments diameter (a), filaments homogeneity (b) and deposition time (c).

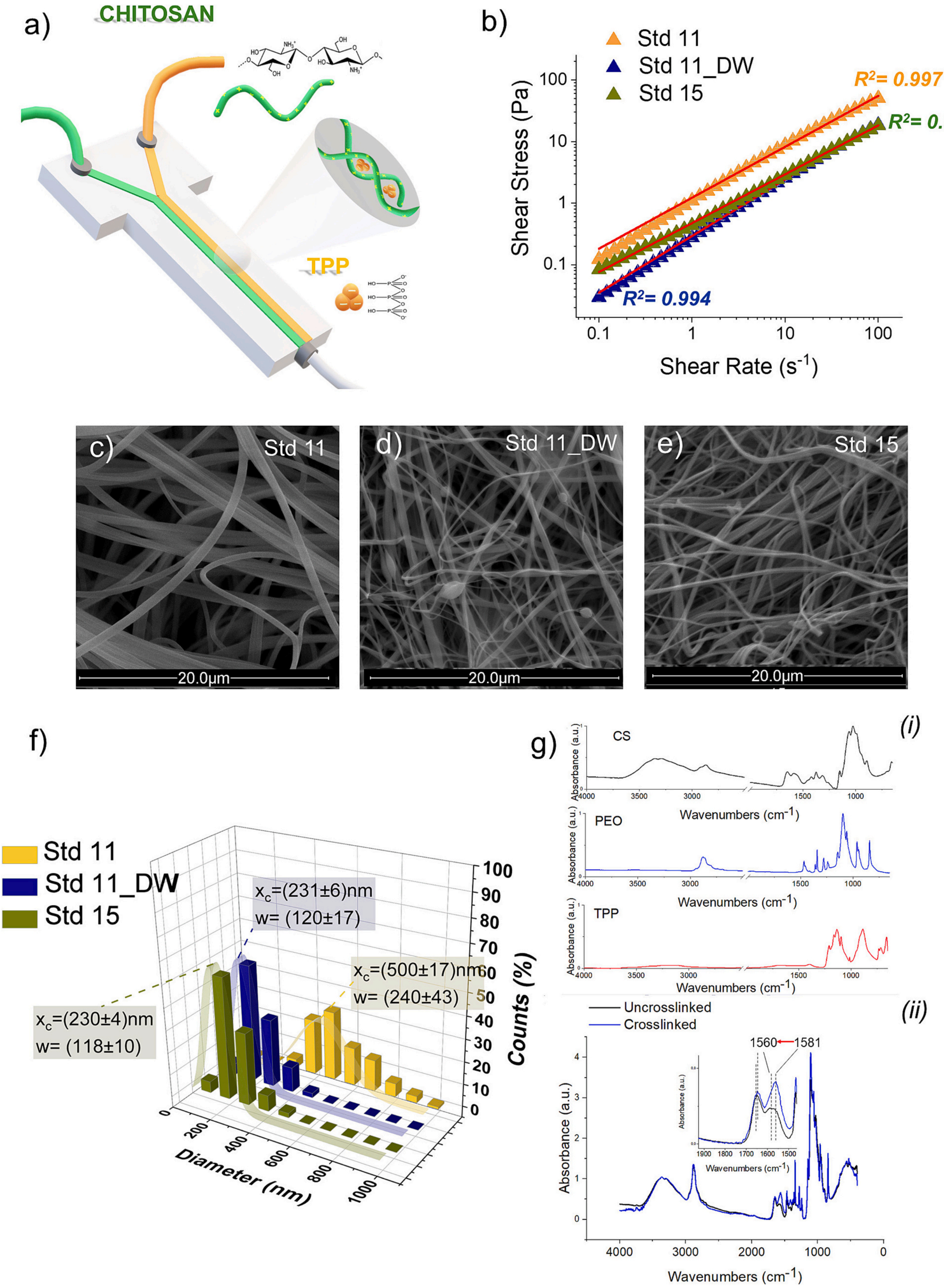

Fig. 5. a) Schematic representation of the microfluidic crosslinking, b) Shear stress – shear rate curves of uncrosslinked (Std11), uncrosslinked and diluted (Std11_DW) and crosslinked samples (Std15), and related R^2 of the Herschel-Bulckely fitting, c) SEM micrograph of uncrosslinked sample obtained using the condition of Std11, d) SEM micrograph of diluted and uncrosslinked sample obtained using the condition of Std11 and distilled water in the crosslinking unit at a FRR 0.5 (Std11_DW), e) SEM micrograph of crosslinked sample obtained using the conditions of Std 15, f) diameter distribution of the Std 11, Std11_DW and Std15, g) FTIR spectra of CS, PEO and TPP and h) detail of the FTIR spectra of uncrosslinked and crosslinked samples.

Table 6
Rheological parameters of the Herschel-Bulkley model.

Herschel-Bulkley model	$\tau = \tau_0 + K\dot{\gamma}^n$ τ_0 = yield stress K = consistency index and n = flow behavior index		
Sample	$K[Pa\ s^n]$	n	R^2
Std 11	1.22 ± 0.07	0.83 ± 0.02	0.979
Std 11_DW	0.293 ± 0.08	0.920 ± 0.009	0.994
Std 15	0.793 ± 0.005	0.47 ± 0.01	0.999

Table 7
Comparison between predicted and experimental results related to the optimized patch.

Optimization Criteria	Selected Conditions	Predicted Results	Experimental Results
$\overline{D}$(nm) target to 300 nm	CS concentration = 3 % (w/V)	$\overline{D}$ (nm) = 297 ± 22	$\overline{D}$ (nm) = 295 ± 12
Minimize w (nm)	FRR_{CR} = 0.25	w (nm)=111 ± 24	w (nm) = 186 ± 25
30 min < Time < 60 min	Pressure = 1.8 Bar	Time (min) = 35 ± 2	Time (min) > 40 min

increased instability of the polymer solution droplet at the capillary tip and reduces the resistance to jet stretching, resulting in thinner nanofilaments with a narrower diameter distribution but a higher occurrence of droplet defects (Fig. 5d and f).

The Std 15 solution exhibited a lower K than Std 11 because of the dilution effect, but a higher K than Std 11_DW, as the crosslinking with TPP generated more interchain interactions. As a result, a more stable polymer solution is achieved at the capillary tip, leading to the spinning of thinner nanofilaments without defects (Fig. 5e and f).

The water stability of the three solutions is presented in **Fig. S4**. After soaking overnight in distilled water, 65 % of the weight from the uncrosslinked samples (Std 11 and Std 11_DW) remained undissolved. In contrast, the crosslinked sample (Std 15) exhibited a higher undissolved fraction of 80 %, due to the enhanced interchain interactions induced by the TPP (Fig. 5a). The crosslinking reaction was also investigated by FTIR analysis. In Fig. 5g **(i)**, the spectra of pure CS, PEO, and TTP are shown. The spectrum of CS shows the characteristic broad adsorption band between 3500 and 3100 cm^{-1} (N—H and O—H stretching vibrations) and the amide peaks at 1650 cm^{-1} (C═O stretching vibration), 1582 cm^{-1} (N—H in plane deformation), and 1378 cm^{-1}. Other significant adsorption bands for CS are in the 1500–1198 cm^{-1} range associated to the -CH2 wagging coupled with the -O-H in plane deformation and in the 1150–1000 cm^{-1} range due to the pyranose ring [22]. The spectrum of PEO shows the spectral band in the 3617–3183 cm^{-1} due to the O—H stretching vibrations, the band at 2883 cm^{-1} related to the C—H bending vibrations and the characteristic triple peak in the 1280–1110 cm^{-1} range, due to the stretching vibrations of the alcoholic O—H and C-O-C ether linkage.

The FTIR spectrum of TPP is characterized by the absorption band at 1211 cm^{-1} due to the P = O stretching, the band at 1130 cm^{-1} attributed to the symmetric and antisymmetric stretching of the -PO_2 group, the band at 1090 cm^{-1} associated to the symmetric and antisymmetric stretching of the PO_3 group and at 881 cm^{-1} attributed to the antisymmetric stretching of the P-O-P bond.

In Fig. 5g **(ii)**, the FTIR spectra of the uncrosslinked and crosslinked samples, normalized for the adsorption band at 1650 cm^{-1} are shown. Both spectra display the characteristic peaks of CS and PEO (Fig. 5 **g (i)**). However, as detailed in the box of Fig. 5g **(ii)**, the peak at 1581 cm^{-1} of the uncrosslinked sample is shifted to 1560 cm^{-1} in the crosslinked one. Moreover, an increased intensity of this peak in the crosslinked sample compared to the uncrosslinked one can be observed. This behavior is attributed to the bonds between the phosphoric groups of TPP and the amino groups in chitosan proving that crosslinking occurred (Fig. 5a) [39].

3.5. Validation of the model

The obtained design spaces (Fig. 4) indicate that filament diameters lower than 300 nm with a great homogeneity (W approaching the 150 nm) can be obtained with a CS concentration approaching 3 % (*w*/*V*) and a pressure approaching 2 bar. Nevertheless, a higher deposition time (> 30 min) can be obtained at a lower FRR_{CR}. To obtain a good compromise between homogeneous nanofilaments and suitable deposition time, the optimization criteria listed in Table 7 were selected to validate the design spaces through the predictive modeling and simulation approach. The software returned a desirability function D, indicating the degree to which all the responses are satisfied. The desirability function varies from 0, meaning that the criteria are not simultaneously satisfied, and 1, meaning that all the criteria are simultaneously satisfied. Based on the desirability function plot (Fig. 6a), the selected conditions to obtain patches with desired optimization criteria were a CS concentration of 3 % (w/V), an FRR_{CR} of 0.25, and a pressure of 1.8 bar (Table 7). In Fig. 6b, the visual image, as well as the SEM image and diameter distribution of the patch obtained using the selected conditions, are shown. As shown in Table 7, for the diameter and the deposition time, the experimental results closely match the theoretical values predicted by the model, confirming the goodness of the model. Instead, a significant discrepancy between the predicted and experimental value emerged for the diameter distribution width. This behavior was expected due to the weakness of the model for outputs lower than 150 nm. To validate the patch obtained with the selected conditions for wound healing purposes, its swelling ability, as well as its water stability, were estimated. As observed in Fig. 6c, the patch immersed in water for 24 h did not lose its fibrous structure, although the filaments appeared swollen. The calculated swelling ratio is 470 ± 60 % and in agreement with the one evaluated by Sarkar et al. [18].

Instead, regarding stability in water, it was observed that about 40 % of the patch dissolves when immersed in water overnight, and this is due to the dissolution of the PEO. Indeed, as can be seen from the FTIR spectra (Fig. 6d) normalized for the band at 1650 cm^{-1}, the adsorption bands attributable to PEO (blue boxes) that are evident in the sample before water treatment disappear in the sample after water treatment.

3.6. Patch biocompatibility

The cytotoxic behavior of the patch was assessed in human HaCaT keratinocyte cells via the WST-8 and SRB assays. This cell line was selected because it has been intensely used as a model for epidermal cells [40,41,42]. Fig. 7a shows that HaCaT cell metabolic activity was normal for the negative control (100 % cell viability) as well as for the patch extractive medium at the three different dilutions, while a strong reduction was observed for the positive control (10 % DMSO) (*p-value* < 0.0001 vs negative control and extractive medium).

The same trend was obtained by the SRB test that evaluates HaCaT cell protein content (Fig. 7b). All values were above the 70 % threshold of cell viability [30], which reflects the potential in vivo performance of these safe and compatible patches for biomedical applications. The optical images of HaCaT cells (Fig. 7c) corroborate the cell viability tests by showing that neither cell morphology nor cell count is altered when compared with the negative control after 24 h of cell incubation with the patch.

4. Conclusion

This study confirms that MBS is an efficient technique for fabricating crosslinked CS nanofibrous for non-woven patches with enhanced structural stability in one single step. By integrating sequential mixing

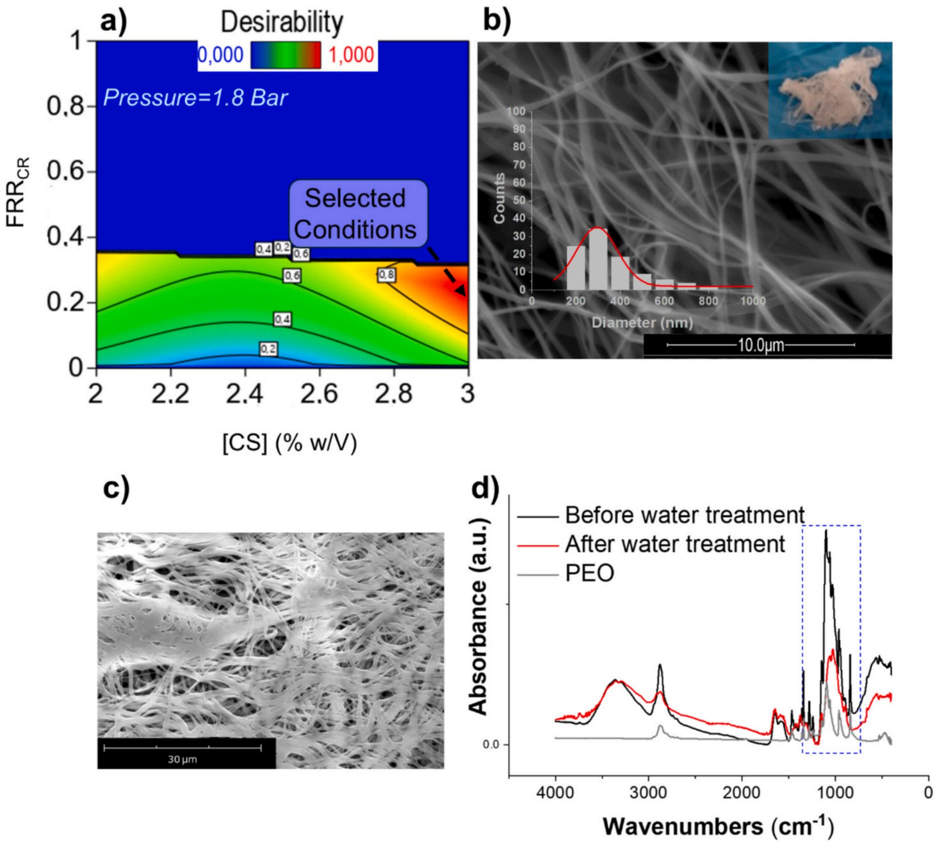

Fig. 6. a) Desirability function plot; b) visual image, SEM images, and diameters distribution of the selected sample; c) SEM image of the patch immersed in water and d) FTIR spectra of the patch before and after water treatment compared with the FTIR spectrum of the PEO.

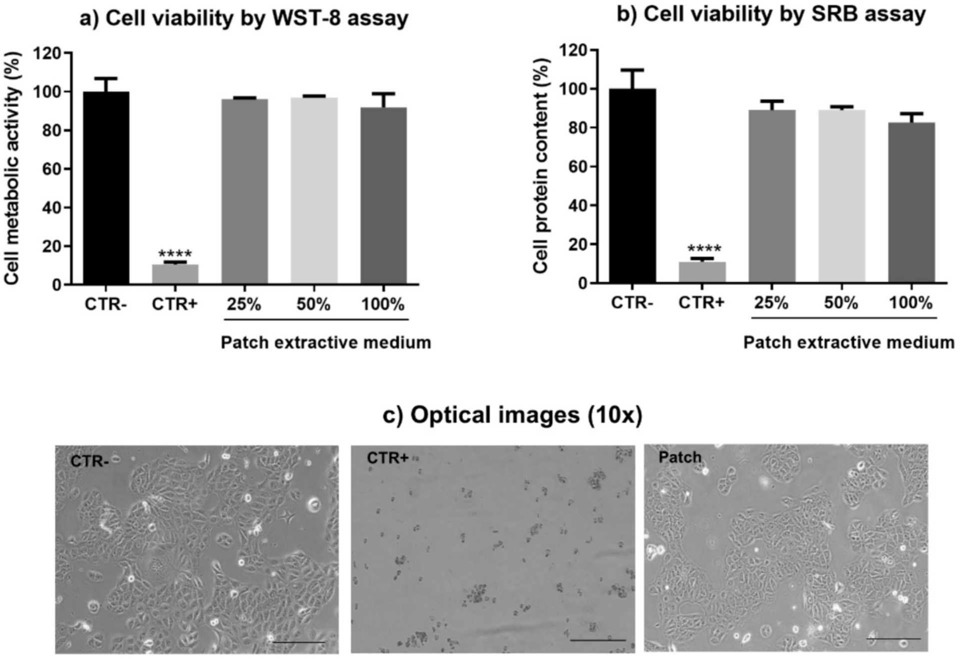

Fig. 7. Cell metabolic activity (a) and cell protein content (b) of HaCaT cells after 24 h of exposure to negative control (complete medium), positive control (10 % DMSO in complete medium) or patch extractive medium at three different dilutions (25–50-100 %), and (c) the corresponding optical images (10×) of HaCaT cells after 24 h of exposure. **** *p*-value <0.0001 vs CTR- and patch extractive medium (Tukey's post-hoc test).

and ionic crosslinking in the pre-spinning phase, the method overcomes the common challenge of phase separation caused by the poor miscibility of CS, PEO, and TPP. This issue limits the use of the traditional solution blow spinning technique. This novel continuous process simplifies fabrication and allows direct in situ deposition of nanofibers by eliminating the need for additional post-processing steps.

Utilizing a DOE approach, mathematical models that correlate various process parameters with patch properties, including filament diameter, homogeneity, and deposition time, were developed and validated.

The obtained results revealed that filament diameter is primarily determined by FRR_{CR} and pressure, fiber homogeneity is strongly influenced by pressure, and deposition time is mainly governed by FRR_{CR}. Crosslinking with TPP enhanced fiber formation by promoting interchain interactions in a less concentrated CS solution, resulting in a more stable polymer solution at the capillary tip. This produced thinner fibers with fewer defects. FTIR analysis confirmed ionotropic crosslinking between the phosphoric groups of TPP and the amino groups of chitosan. Additionally, water stability improved, with weight retention increasing from 65 % in the uncrosslinked samples to 80 % in the crosslinked samples. The spun CS patch also showed no significant cytotoxic effects on HaCaT cells. The design spaces created through the QbD approach can be used as a robust platform for optimizing process conditions to achieve chitosan filaments with customized physical and chemical properties.

Future work will focus on exploring practical applications of this platform for drug delivery, including different encapsulation strategies like direct blending to enable tailored drug release profiles and enhance the wound healing capabilities of the patches. In vitro wound healing, mechanical testing, and drug release studies will be carried out to evaluate the performance. Additionally, the influence of the partial weight loss observed in the patches will be investigated to assess its impact on sustained release and applications that require structural integrity maintenance.

Supplementary data to this article can be found online at https://doi.org/10.1016/j.ijbiomac.2025.146279.

CRediT authorship contribution statement

Ana Filipa Matos: Writing – original draft, Methodology, Investigation, Formal analysis, Data curation. **Alessio Pricci:** Writing – original draft, Methodology, Investigation, Formal analysis, Data curation. **Serena Benedetti:** Writing – original draft, Methodology, Investigation, Formal analysis. **Mattia Tiboni:** Writing – review & editing, Methodology, Data curation. **Annalisa Aluigi:** Writing – review & editing, Writing – original draft, Supervision, Methodology, Formal analysis, Data curation, Conceptualization. **Luca Casettari:** Writing – review & editing, Supervision, Resources, Project administration, Funding acquisition.

Declaration of competing interest

The authors declare that they have no known competing financial interests or personal relationships that could have appeared to influence the work reported in this paper.

Acknowledgments

This work has been funded by the European Union - NextGenerationEU, Mission 4, Component 2, under the Italian Ministry of University and Research (MUR) National Innovation Ecosystem grant ECS00000041 - VITALITY - CUP H33C22000430006.

The authors thank Dr. Laura Valentini (Department of Biomolecular Sciences, University of Urbino Carlo Bo) for the SEM images.

Data availability

Data will be made available on request.

References

[1] Z. Zhou, C. Li, Y. Zeng, T. Huang, X. Jiang, D.-G. Yu, K. Wang, Natural polymer nanofiber dressings for effective management of chronic diabetic wounds: a comprehensive review, Int. J. Biol. Macromol. 282 (2024) 136688, https://doi.org/10.1016/j.ijbiomac.2024.136688.

[2] A. Memic, T. Abdullah, H.S. Mohammed, K. Joshi Navare, T. Colombani, S. A. Bencherif, Latest Progress in electrospun nanofibers for wound healing applications, ACS Appl Bio Mater 2 (2019) 952–969, https://doi.org/10.1021/acsabm.8b00637.

[3] D.K. Patel, S.-Y. Won, E. Jung, S.S. Han, Recent progress in biopolymer-based electrospun nanofibers and their potential biomedical applications: a review, Int. J. Biol. Macromol. 293 (2025) 139426, https://doi.org/10.1016/j.ijbiomac.2024.139426.

[4] S.N. Kalva, R. Augustine, A. Al Mamun, Y.B. Dalvi, N. Vijay, A. Hasan, Active agents loaded extracellular matrix mimetic electrospun membranes for wound healing applications, J. Drug Deliv. Sci. Technol. 63 (2021) 102500, https://doi.org/10.1016/j.jddst.2021.102500.

[5] S. Wen, H. Zhao, Y. Zhang, D. Cao, M. Liu, H. Yang, W. Zhang, Multifunctional nanofiber membranes constructed by microfluidic blow-spinning to inhibit scar formation at early intervention stage, ACS Appl. Mater. Interfaces 16 (2024) 53042–53059, https://doi.org/10.1021/acsami.4c13561.

[6] J.L. Daristotle, A.M. Behrens, A.D. Sandler, P. Kofinas, A review of the fundamental principles and applications of solution blow spinning, ACS Appl. Mater. Interfaces 8 (2016) 34951–34963, https://doi.org/10.1021/acsami.6b12994.

[7] T.S. Demina, E.N. Bolbasov, M.A. Peshkova, Y.M. Efremov, P.Y. Bikmulina, A. V. Birdibekova, T.N. Popyrina, N.V. Kosheleva, S.I. Tverdokhlebov, P.S. Timashev, T.A. Akopova, Electrospinning vs. electro-assisted solution blow spinning for fabrication of fibrous scaffolds for tissue engineering, Polymers (Basel) 14 (2022) 5254, https://doi.org/10.3390/polym14235254.

[8] J. Ahmed, M. Gultekinoglu, M. Edirisinghe, Recent developments in the use of centrifugal spinning and pressurized gyration for biomedical applications, WIREs Nanomedicine and Nanobiotechnology 16 (2024), https://doi.org/10.1002/wnan.1916.

[9] E. Szymańska, M. Wojasiński, R. Czarnomysy, R. Dębowska, I. Łopianiak, K. Adasiewicz, T. Ciach, K. Winnicka, Chitosan-enriched solution blow spun poly (ethylene oxide) nanofibers with poly(Dimethylsiloxane) hydrophobic outer layer for skin healing and regeneration, Int. J. Mol. Sci. 23 (2022) 5135, https://doi.org/10.3390/ijms23095135.

[10] B.S. de Farias, T.R. Sant'Anna Cadaval Junior, L.A. de Almeida Pinto, Chitosan-functionalized nanofibers: a comprehensive review on challenges and prospects for food applications, Int. J. Biol. Macromol. 123 (2019) 210–220, https://doi.org/10.1016/j.ijbiomac.2018.11.042.

[11] X. Chen, H. Huang, X. Song, T. Dong, J. Yu, J. Xu, R. Cheng, T. Cui, J. Li, Carboxymethyl chitosan-based hydrogel-Janus nanofiber scaffolds with unidirectional storage-drainage of biofluid for accelerating full-thickness wound healing, Carbohydr. Polym. 331 (2024) 121870, https://doi.org/10.1016/j.carbpol.2024.121870.

[12] M. Khodadadi Yazdi, F. Seidi, A. Hejna, P. Zarrintaj, N. Rabiee, J. Kucinska-Lipka, M.R. Saeb, S.A. Bencherif, Tailor-made polysaccharides for biomedical applications, ACS Appl. Bio Mater. 7 (2024) 4193–4230, https://doi.org/10.1021/acsabm.3c01199.

[13] E. Szymanska, R. Czarnomysy, J. Jacyna, A. Basa, A.Z. Wilczewska, M. Markuszewski, K. Winnicka, Could spray-dried microbeads with chitosan glutamate be considered as promising vaginal microbicide carriers? The effect of process variables on the in vitro functional and physicochemical characteristics, Int J Pharm 568 (2019) 118558 https://doi.org/10.1016/j.ijpharm.2019.118558.

[14] N.D. Tien, T. Geng, C.A. Heyward, J.E. Reseland, S.P. Lyngstadaas, J.J. Blaker, H. J. Haugen, Solution blow spinning of highly deacetylated chitosan nanofiber scaffolds for dermal wound healing, Biomaterials Advances 137 (2022) 212871, https://doi.org/10.1016/j.bioadv.2022.212871.

[15] P. Kianfar, A. Vitale, S. Dalle Vacche, R. Bongiovanni, Photo-crosslinking of chitosan/poly(ethylene oxide) electrospun nanofibers, Carbohydr. Polym. 217 (2019) 144–151, https://doi.org/10.1016/j.carbpol.2019.04.062.

[16] M. Pakravan, M.-C. Heuzey, A. Ajji, Determination of phase behavior of poly (ethylene oxide) and chitosan solution blends using Rheometry, Macromolecules 45 (2012) 7621–7633, https://doi.org/10.1021/ma301193h.

[17] Z. Qin, X. Jia, Q. Liu, B. Kong, H. Wang, Enhancing physical properties of chitosan/pullulan electrospinning nanofibers via green crosslinking strategies, Carbohydr. Polym. 247 (2020) 116734, https://doi.org/10.1016/j.carbpol.2020.116734.

[18] S.D. Sarkar, B.L. Farrugia, T.R. Dargaville, S. Dhara, Physico-chemical/biological properties of tripolyphosphate cross-linked chitosan based nanofibers, Mater. Sci. Eng. C 33 (2013) 1446–1454, https://doi.org/10.1016/j.msec.2012.12.066.

[19] W.-H. Lin, W.-B. Tsai, *In situ* UV-crosslinking gelatin electrospun fibers for tissue engineering applications, Biofabrication 5 (2013) 035008, https://doi.org/10.1088/1758-5082/5/3/035008.

[20] G. Maurizii, S. Moroni, J.V. Jimènez Núnez, G. Curzi, M. Tiboni, A. Aluigi, L. Casettari, Non-invasive peptides delivery using chitosan nanoparticles assembled via scalable microfluidic technology, Carbohydrate Polymer Technologies and Applications 7 (2024) 100424, https://doi.org/10.1016/j.carpta.2024.100424.

[21] A. Woźniak, M. Biernat, Methods for crosslinking and stabilization of chitosan structures for potential medical applications, J. Bioact. Compat. Polym. 37 (2022) 151–167, https://doi.org/10.1177/08839115221085738.

[22] I. Silvestro, I. Francolini, V. Di Lisio, A. Martinelli, L. Pietrelli, A. Scotto d'Abusco, A. Scoppio, A. Piozzi, Preparation and characterization of TPP-chitosan crosslinked

scaffolds for tissue engineering, Materials 13 (2020) 3577, https://doi.org/10.3390/ma13163577.

[23] S.D. Sarkar, B.L. Farrugia, T.R. Dargaville, S. Dhara, Physico-chemical/biological properties of tripolyphosphate cross-linked chitosan based nanofibers, Mater. Sci. Eng. C 33 (2013) 1446–1454, https://doi.org/10.1016/j.msec.2012.12.066.

[24] D. Izzo, B. Palazzo, F. Scalera, F. Gullotta, V. lapesa, S. Scialla, A. Sannino, F. Gervaso, Chitosan scaffolds for cartilage regeneration: influence of different ionic crosslinkers on biomaterial properties, Int. J. Polym. Mater. Polym. Biomater. 68 (2019) 936–945, https://doi.org/10.1080/00914037.2018.1525538.

[25] B.S. de Farias, T.R. Sant'Anna Cadaval Junior, L.A. de Almeida Pinto, Chitosan-functionalized nanofibers: a comprehensive review on challenges and prospects for food applications, Int. J. Biol. Macromol. 123 (2019) 210–220, https://doi.org/10.1016/j.ijbiomac.2018.11.042.

[26] D. de O. Maionchi, L. Ainstein, F.P. dos Santos, M.B. de Souza Júnior, Computational fluid dynamics and machine learning as tools for optimization of micromixers geometry, Int, J Heat Mass Transf 194 (2022) 123110, https://doi.org/10.1016/j.ijheatmasstransfer.2022.123110.

[27] A. Kasemiire, H.T. Avohou, C. De Bleye, P.-Y. Sacre, E. Dumont, P. Hubert, E. Ziemons, Design of experiments and design space approaches in the pharmaceutical bioprocess optimization, Eur. J. Pharm. Biopharm. 166 (2021) 144–154, https://doi.org/10.1016/j.ejpb.2021.06.004.

[28] S. Khorshid, R. Goffi, G. Maurizii, S. Benedetti, G. Sotgiu, R. Zamboni, S. Buoso, R. Galuppi, T. Bordoni, M. Tiboni, A. Aluigi, L. Casettari, Microfluidic manufacturing of tioconazole loaded keratin nanocarriers: development and optimization by design of experiments, Int. J. Pharm. 647 (2023) 123489, https://doi.org/10.1016/j.ijpharm.2023.123489.

[29] G. Maurizii, L. Valentini, G. Sotgiu, R. Zamboni, C. Tonetti, C. Vineis, B. Canonico, M. Montanari, M. Tiboni, L. Casettari, A. Aluigi, The dark side of the wool? From wool wastes to keratin microfilaments through the solution blow spinning process, Int. J. Biol. Macromol. 275 (2024) 133722, https://doi.org/10.1016/j.ijbiomac.2024.133722.

[30] ISO 10993-5:2009(E), Biological Evaluation of Medical Devices - Part 5, in: Tests for In Vitro Cytotoxicity; ISO: Geneva, Switzerland, 2009 n.d.

[31] S. Benedetti, M.G. Nasoni, F. Luchetti, F. Palma, New insights into the cytotoxic effects of Thymus vulgaris essential oil on the human triple-negative breast cancer cell line MDA-MB-231, Toxicol. in Vitro 93 (2023) 105705, https://doi.org/10.1016/j.tiv.2023.105705.

[32] B. Elarbe, I. Elganidi, N. Ridzuan, K. Yusoh, N. Abdullah, S. Vijaya Kumar, Application of full factorial design to screen the factors influencing the wax deposition of Malaysian crude oil, J. Pet. Explor. Prod. Technol. 12 (2022) 1829–1839, https://doi.org/10.1007/s13202-021-01431-8.

[33] G.C. Dadol, A. Kilic, L.D. Tijing, K.J.A. Lim, L.K. Cabatingan, N.P.B. Tan, E. Stojanovska, Y. Polat, Solution blow spinning (SBS) and SBS-spun nanofibers: materials, methods, and applications, Mater Today Commun 25 (2020) 101656, https://doi.org/10.1016/j.mtcomm.2020.101656.

[34] J. Li, G. Song, J. Yu, Y. Wang, J. Zhu, Z. Hu, Preparation of solution blown Polyamic acid nanofibers and their Imidization into polyimide nanofiber Mats, Nanomaterials 7 (2017) 395, https://doi.org/10.3390/nano7110395.

[35] J. An, H. Zhang, J. Zhang, Y. Zhao, X. Yuan, Preparation and antibacterial activity of electrospun chitosan/poly(ethylene oxide) membranes containing silver nanoparticles, Colloid Polym. Sci. 287 (2009) 1425–1434, https://doi.org/10.1007/s00396-009-2108-y.

[36] M.Á.V. Rodrigues, M.R.V. Bertolo, M.M. Horn, A.B. Lugão, L.H.C. Mattoso, A.M. de Guzzi Plepis, Comparing solution blow spinning and electrospinning methods to produce collagen and gelatin ultrathin fibers: a review, Int. J. Biol. Macromol. 283 (2024) 137806, https://doi.org/10.1016/j.ijbiomac.2024.137806.

[37] J.L. Daristotle, A.M. Behrens, A.D. Sandler, P. Kofinas, A review of the fundamental principles and applications of solution blow spinning, ACS Appl. Mater. Interfaces 8 (2016) 34951–34963, https://doi.org/10.1021/acsami.6b12994.

[38] M. Gierszewska, J. Ostrowska-Czubenko, Chitosan-based membranes with different ionic crosslinking density for pharmaceutical and industrial applications, Carbohydr. Polym. 153 (2016) 501–511, https://doi.org/10.1016/j.carbpol.2016.07.126.

[39] D.R. Bhumkar, V.B. Pokharkar, Studies on effect of pH on cross-linking of chitosan with sodium tripolyphosphate: a technical note, AAPS PharmSciTech 7 (2006) E138–E143, https://doi.org/10.1208/pt070250.

[40] D.F.S. Fonseca, J.P.F. Carvalho, V. Bastos, H. Oliveira, C. Moreirinha, A. Almeida, A.J.D. Silvestre, C. Vilela, C.S.R. Freire, Antibacterial multi-layered nanocellulose-based patches loaded with Dexpanthenol for wound healing applications, Nanomaterials 10 (2020) 2469, https://doi.org/10.3390/nano10122469.

[41] J.P.F. Carvalho, A.C.Q. Silva, V. Bastos, H. Oliveira, R.J.B. Pinto, A.J.D. Silvestre, C. Vilela, C.S.R. Freire, Nanocellulose-based patches loaded with hyaluronic acid and diclofenac towards aphthous stomatitis treatment, Nanomaterials 10 (2020) 628, https://doi.org/10.3390/nano10040628.

[42] M. Contardi, M. Summa, P. Picone, O.R. Brancato, Di M. Carlo, R. Bertorelli, A. Athanassiou, Evaluation of a multifunctional polyvinylpyrrolidone/hyaluronic acid-based bilayer film patch with anti-inflammatory properties as an enhancer of the wound healing process Pharmaceutics, 14, 2022, p. 483, https://doi.org/10.3390/pharmaceutics14030483.